Multiple plasmonic-photonic couplings in the Au nanobeaker arrays: enhanced robustness and wavelength tunability

Linhan Lin and Yuebing Zheng*

Department of Mechanical Engineering, Materials Science & Engineering Program, and Texas Materials Institute, The University of Texas at Austin, Austin, Texas 78712, USA

**Corresponding author: zheng@austin.utexas.edu*

Received March 18, 2015; revised April 10, 2015; accepted April 11, 2015; posted April 13, 2015 (Doc. ID 236389); published April 29, 2015

Diffractive coupling in the plasmonic nanoparticle arrays introduces the collective plasmon resonances with high scattering efficiency and narrow linewidth. However, the collective plasmon resonances can be suppressed when the arrays are supported on the solid-state substrates with different superstrates because of the different dispersion relations between the substrate and the superstrate. Herein, we develop a general concept which seeks to synergize the subnanoparticle engineering of "hot spots" with the far-field coupling behavior, for the versatile control of plasmonic-photonic couplings in an asymmetric environment. To demonstrate our concept, we choose as an example the Au nanobeaker arrays (NBAs), which are the conformally coated Au thin layers on the interior sidewalls and bottoms of nanohole arrays in SiO_2 substrates. Using the finite-difference time-domain simulations, we show that engineering the plasmonic "hot spots" in the NBAs by simply controlling the depth-to-diameter aspect ratio of individual units enables multiple plasmonic-photonic couplings in an asymmetric environment. These couplings are robust with a wide range of resonance wavelengths from visible to infrared. Furthermore, the angle-dependent transmission spectra of the arrays reveal a transition from band-edge to propagating state for the orthogonal coupling and a splitting of diffraction waves in the parallel coupling. The proposed NBAs will find enhanced applications in plasmonic lasers and biosensing.

OCIS codes: (260.3910) Metal optics; (240.6680) Surface plasmons; (260.5740) Resonance; (160.4236) Nanomaterials.
http://dx.doi.org/10.1364/OL.40.002060

Plasmonic nanoparticles that support localized surface plasmon resonances (LSPRs) exhibit extraordinary optical field confinement [1–6]. The nanoparticle arrays can further increase the field enhancement and suppress the radiative damping due to the plasmonic-photonic coupling, leading to the lattice plasmon resonances (LPRs) [7–10]. The LPRs have been studied both theoretically and experimentally [11–20], with targeted applications in plasmonic laser [21,22] and biosensing [23–25] that benefit from the high-quality factor in the extinction spectra. One of the major challenges with the plasmonic-photonic coupling is its requirement of a homogeneous refractive index environment for the nanoparticle arrays. The LPRs are suppressed when the particle arrays are supported on a substrate, which has different refractive index from that of the superstrate, as required for many applications. The asymmetric substrate–superstrate environment cuts off the diffraction orders at the interface [26]. Recently, the larger nanoparticles with an increased polarizability have been demonstrated to maintain the LPRs in an asymmetric environment [19,27]. However, the LPRs in the arrays of these larger nanoparticles occur for a narrow range of resonance wavelengths with the reduced tunability.

In this Letter, we demonstrate that Au nanobeaker arrays (NBAs), which are the conformally coated Au thin layers on the interior sidewalls and bottoms of nanohole arrays in SiO_2 substrates, enable multiple plasmonic-photonic couplings that are robust and highly tunable in an asymmetric environment. While most of the previously studied nanoparticle arrays (nanodisk [18,19,27] or nanorod [16] arrays) support the plasmonic "hot spots" at the particles-substrate interface, the nanobeaker structure can confine the "hot spots" within the substrate to couple strongly with the substrate diffraction orders, leading to the robust orthogonal plasmonic-photonic coupling in an asymmetric environment. Also, different from the commonly studied nanohole arrays in metal films [28,29], where the coupling between the surface plasmon polariton (SPP) and the diffraction orders occurs, the NBAs support the coupling between the LSPRs and the diffraction orders. We can further achieve subnanoparticle-scale manipulation of the "hot spots" associated with the higher order modes of LSPRs through controlling the depth-to-diameter aspect ratio of individual nanobeakers. These higher order modes of LSPRs allow the plasmonic-photonic couplings at different diffraction orders. We further understand the physical principles of the couplings by studying the dispersion relations of the LPRs based on the angle-dependent transmission spectra. All our calculations are based on finite-difference time-domain (FDTD) method using commercial software (FDTD solution, Lumerical Inc.).

The Au NBAs are schematically displayed in Fig. 1(a). The Au nanoshells have the thickness of 20 nm, the inner diameter of $D = 50$ or 150 nm, and the depth of h ranging from 50 to 200 nm. The optical constants of Au were taken from Johnson and Christy [30] in the FDTD calculations. The refractive index of SiO_2 substrate and air with $n_{sub} = 1.44$ and $n_{sup} = 1.0$ are chosen to generate an asymmetric environment. The wavelength of the diffraction orders is tuned by controlling the lattice constants of the NBAs according to the following equation [31]:

$$\left(k_x \pm i\frac{2\pi}{a_x}\right)^2 + \left(k_y \pm j\frac{2\pi}{a_y}\right)^2 = k^2, \quad (1)$$

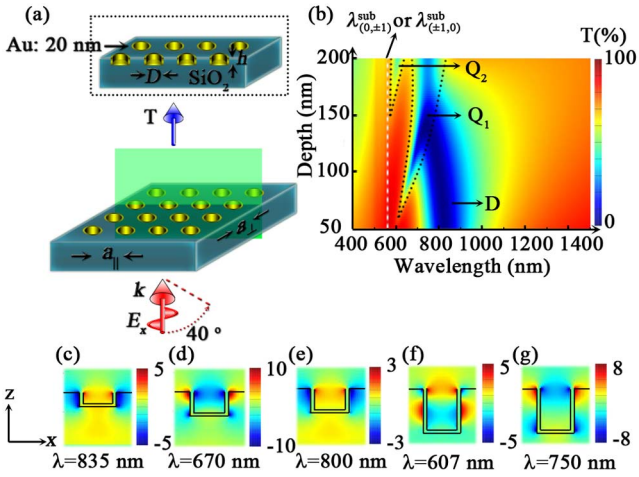

Fig. 1. (a) Schematic of the Au NBAs on the SiO_2 substrate. The incident light is launched from the substrate with E_x polarization and the incident angle from 0° to 40°. The transmission light is collected above the structure. $a_{\parallel}$ and $a_{\perp}$ indicate the lattice constants that are parallel and vertical to the polarization direction of the incident light, respectively. The inset shows the cross-section of the NBAs. h is the depth of the nanobeaker, and D is the diameter of the nanohole after the Au deposition. (b) The simulated transmission spectra of the NBAs as a function of the depth at $a_{\parallel} = a_{\perp} = 400$ nm. The diffraction orders $\lambda^{\mathrm{sub}}_{(0,\pm1)}$ and $\lambda^{\mathrm{sub}}_{(\pm1,0)}$, and the different modes of LSPRs are indicated with the dot lines. Distributions of the real parts of E_x in the xz plane through the center of the nanobeaker with (c) $h = 50$ nm; (d), (e) $h = 100$ nm; (f), (g) $h = 200$ nm.

where k_x and k_y are the in-plane wave number along x and y axis, respectively. i and j are integers. a_x and a_y indicate the lattice constants along x and y axis, which corresponds to $a_{\parallel}$ and $a_{\perp}$ of the NBAs indicated in Fig. 1(a). k is the wave number of the in-plane propagating diffraction waves. Assuming the light is incident at an angle θ, the diffraction condition becomes

$$\left(\sin\theta \pm i\frac{\lambda}{na_x}\right)^2 + \left(\pm j\frac{\lambda}{na_y}\right)^2 = 1, \tag{2}$$

where n is the refractive index of the media surrounding the structure, and λ is the wavelength of the incident light. Therefore, the $(\pm i, 0)$ and $(0, \pm j)$ diffraction orders can be described as

$$\lambda_{(\pm i,0)} = n\frac{1\mp\sin\theta}{i}a_x \quad \text{and} \quad \lambda_{(0,\pm j)} = n\frac{\cos\theta}{j}a_y. \tag{3}$$

Depending on the refractive index, two sets of diffraction orders are obtained in an asymmetric structure, with $\lambda^{\mathrm{sub}}_{(i,j)}$ and $\lambda^{\mathrm{sup}}_{(i,j)}$ indicating the (i, j) substrate and superstrate diffraction orders, respectively.

To examine the distributions of "hot spots" in the NBAs with different depth-to-diameter aspect ratios, we simulated the transmission spectra of the arrays under normal illumination as a function of the depth h, as shown in Fig. 1(b). For this purpose, the lattice constants $a_x = a_y = 400$ nm are chosen to tune the diffraction orders to the higher energy side of the LSPRs to eliminate the plasmonic-photonic coupling. When the depth is 50 nm, a single-dipole-bonding mode (D mode) with the resonance wavelength at 835 nm is observed. A pair of "hot spots" is located on both sides of the nanobeaker within the substrate, while another pair is located on the inner sides of the nanobeaker in the superstrate. Due to the phase retardation, the increase of the depth introduces higher order resonance modes, i.e., quadrupole modes. The NBAs with $h = 100$ nm show the D mode at 800 nm and a quadrupole modes (Q_1 mode) at 670 nm, with the corresponding "hot spots" distributions listed in Figs. 1(d) and 1(e), respectively. The increase of the depth pushes the "hot spots" of the D mode to the interface, and the decrease of the effective refractive index surrounding the "hot spots" causes a slight blueshift of the resonance wavelength. Further increase of the depth leads to the decrease of the resonance strength and D mode disappears in the transmission spectrum when $h = 200$ nm. However, it is confirmed in both the reflection spectra (not shown here) and the orthogonal coupling behavior [Fig. 2(c)] that the D mode is still maintained at the longer wavelength. Furthermore, a redshift of the Q_1 mode and the emergence of another quadrupole mode (Q_2 mode) are observed when $h = 200$ nm. Different from the Q_1 mode, where the "hot spots" are located at both top and bottom parts of the nanobeaker [Fig. 1(g)], the Q_2 mode at the shorter wavelength possesses the "hot spots" on both sides of the nanobeaker, as well as the "hot spots" in the inner sides of the nanobeaker at the top. This engineering of "hot spots" locations by controlling the aspect ratio provides the opportunity to generate new plasmonic-photonic couplings in the NBAs.

Figures 2(a)–2(c) demonstrate the orthogonal coupling behavior of the NBAs with $D = 150$ nm and $h = 50$, 100, and 150 nm, respectively. A robust coupling between the D_1 mode and $\lambda^{\mathrm{sub}}_{(0,\pm1)}$ is observed, with a narrow linewidth obtained when $\lambda^{\mathrm{sub}}_{(0,\pm1)}$ overlaps with the resonance wavelength of the D_1 mode. The narrow transmission dips redshift when the depth increases because the D mode is maintained at longer wavelength. A significant coupling is also observed between the D_1 mode and $\lambda^{\mathrm{sub}}_{(0,\pm2)}$. The lattice constants around 1400 nm indicate the possibility to obtain the plasmonic-photonic coupling in

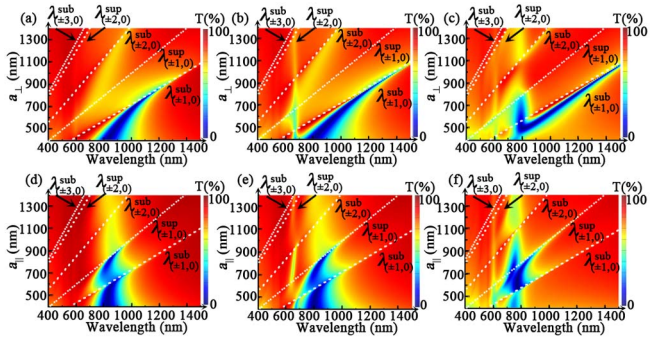

Fig. 2. Simulated transmission spectra of the Au NBAs as a function of the lattice constants with (a)–(c) $a_{\parallel} = 400$ nm, and (a) $h = 50$ nm, (b) $h = 100$ nm, (c) $h = 200$ nm, (d)–(f) $a_{\perp} = 400$ nm, and (d) $h = 50$ nm, (e) $h = 100$ nm, (f) $h = 200$ nm. The diffraction orders are indicated with the dotted lines.

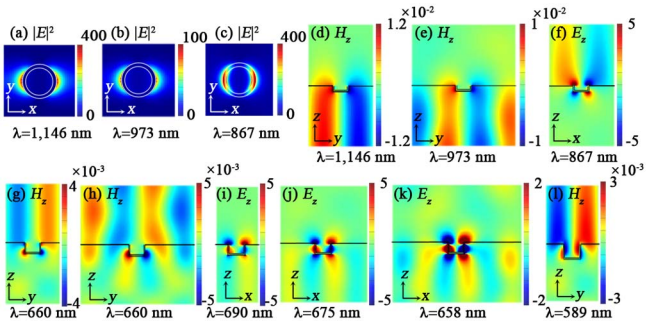

Fig. 3. Electromagnetic field distributions in the Au NBAs with (a), (d) $a_{\parallel} = 400$ nm, $a_{\perp} = 820$ nm, $h = 50$ nm, (b), (e) $a_{\parallel} = 400$ nm, $a_{\perp} = 1400$ nm, $h = 50$ nm, (c), (f) $a_{\parallel} = 860$ nm, $a_{\perp} = 400$ nm, $h = 50$ nm, (g) $a_{\parallel} = 400$ nm, $a_{\perp} = 660$ nm, $h = 100$ nm, (h) $a_{\parallel} = 400$ nm, $a_{\perp} = 1330$ nm, $h = 100$ nm, (i) $a_{\parallel} = 490$ nm, $a_{\perp} = 400$ nm, $h = 100$ nm, (j) $a_{\parallel} = 960$ nm, $a_{\perp} = 400$ nm, $h = 100$ nm, (k) $a_{\parallel} = 1400$ nm, $a_{\perp} = 400$ nm, $h = 100$ nm, (l) $a_{\parallel} = 400$ nm, $a_{\perp} = 590$ nm, $h = 200$ nm. The xy plane in (c) is located 5 nm above the nanobeaker, while the planes in other panels cross through the center of the nanobeaker.

the arrays with micro-scale lattice constants. The orthogonal coupling can be explained using the coupled dipole theory. The in-plane propagating magnetic field in the diffraction waves [Figs. 3(d) and 3(e)] induces the retarded electric field and enhances the intensity of the dipolar "hot spots" [Figs. 3(a) and 3(b)]. However, the intensity enhancement under higher order coupling is lower, which is attributed to the lower density of the near-field "hot spots." The coupling between the D mode and the superstrate diffraction orders is not observed in the NBAs with low aspect ratio. However, the engineering of the "hot spots" locations by increasing the aspect ratio can significantly modify this coupling behavior since the "hot spots" are pushed toward the interface, and the coupling with the superstrate diffraction orders is enabled. When the depth is 100 nm [Fig. 2(b)], the "hot spots" located at the superstrate–substrate interface in the Q_1 mode couple with the superstrate diffraction orders, i.e., $\lambda^{\mathrm{sup}}_{(0,\pm1)}$ and $\lambda^{\mathrm{sup}}_{(0,\pm2)}$. This coupling behavior is observed in Figs. 3(g) and 3(h), with the H_z component extended from the interface into the superstrate. The Q_2 mode generated at $h = 200$ nm can also couple with the superstrate diffraction orders orthogonally [Fig. 2(c)], with the coupling behavior displayed in Fig. 3(l). This high-aspect-ratio-enabled coupling allows the generation of the LPRs in the NBAs with different lattice constants, ranging from 600 to 1400 nm. It should be noted that the couplings between the LSPRs and the higher order diffraction modes are weak and can be easily suppressed by the substrate in the traditional Au nanoparticle arrays. However, the specific "hot spots" distributions in the NBAs make it possible to maintain these couplings in an asymmetric environment.

Parallel coupling is also observed in these NBAs, with the D mode coupling strongly with $\lambda^{\mathrm{sup}}_{(\pm1,0)}$. A weak coupling between the D mode and $\lambda^{\mathrm{sub}}_{(\pm1,0)}$ is also obtained. Different from the orthogonal coupling, the horizontally propagating electric field in the diffraction waves [Fig. 3(f)] directly causes the out-of-plane resonance and induces the out-of-plane "hot spots," without enhancing the dipole intensity of the D mode. A concentrated electric field above the nanobeakers caused by the out-of-plane resonance is displayed in Fig. 3(c). The introduction of the quadrupole mode creates the "hot spots" at the bottom sides of the nanobeakers, which enable the coupling with the substrate diffraction orders [Fig. 2(e)]. The coupling behavior of the Q_1 mode with $\lambda^{\mathrm{sub}}_{(\pm1,0)}$, $\lambda^{\mathrm{sub}}_{(\pm2,0)}$, and $\lambda^{\mathrm{sub}}_{(\pm3,0)}$ are shown in Figs. 3(i), 3(j), and 3(k), respectively, with the in-plane propagating electric field strengthening the out-of-plane "hot spots" in E_z.

For the LPRs in the previously reported Au nanoparticles arrays [26,27], large particle size is required to increase the polarizability and maintain the plasmonic-photonic coupling in an asymmetric environment, which restricts the LPRs in the near-infrared regime. However, the design of the NBAs shows extremely robust LPRs when the diameter of the nanobeaker is significantly decreased, indicating that the suppression by the substrate is eliminated due to the unique "hot spots" locations shown in Fig. 1. In order to verify this supposition, the transmission spectra of the NBAs with $D = 50$ nm as a function of the lattice constants are simulated, as shown in Fig. 4. Robust coupling between the D mode and both $\lambda^{\mathrm{sub}}_{(0,\pm1)}$ and $\lambda^{\mathrm{sub}}_{(0,\pm2)}$ is well maintained [Fig. 4(a)], with the resonance wavelength located in the visible range. Furthermore, the parallel coupling between the D mode and the superstrate diffraction orders is also observed when the diameter is down to 50 nm. This indicates that the resonance wavelength of both the orthogonal and parallel LPRs can be tuned from visible to near-infrared by controlling the diameter of the nanobeakers.

In order to investigate the dispersion relations of the LPRs in the NBAs, the angle-dependent transmission spectra are shown in Fig. 5. Different dispersion properties between the orthogonal and parallel coupling are revealed. In the orthogonal coupling, a blueshift of the resonance wavelength is observed when the incident angle is increased. According to Eq. (3), $\lambda^{\mathrm{sub}}_{(0,\pm1)}$ are proportional to $\cos\theta$, thus the increase of θ leads to the blueshift of the diffraction orders [indicated with the dot line in Fig. 5(a)]. Since the linewidth of D mode is broad, the coupling can be maintained within a wide range of incident angles. It is also observed that the LPRs evolve from a band edge state (with near-zero group velocity at small incident angle) to a propagating state (large incident angle). Specifically, the band edge state with low group velocity is preferred for applications in plasmonic lasers to enhance the quality factor. In contrast, a splitting of $\lambda^{\mathrm{sub}}_{(\pm1,0)}$ is observed in the parallel coupling. The increase

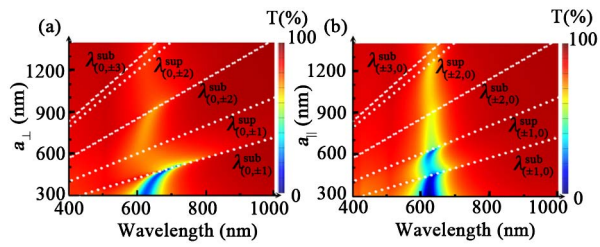

Fig. 4. Simulated transmission spectra of the Au NBAs as a function of the lattice constants with $D = 50$ nm and (a) $a_{\parallel} = 300$ nm, $h = 50$ nm; (b) $a_{\perp} = 300$ nm, $h = 50$ nm.

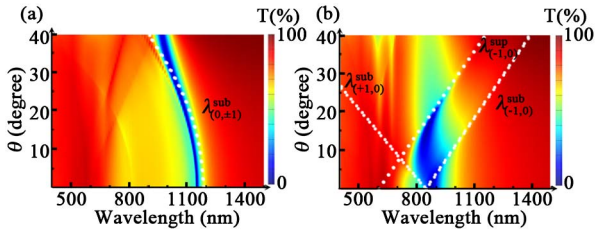

Fig. 5. Simulated transmission spectra of the Au NBAs as a function of the incident angle θ (from 0° to 40°) with $D = 150$ nm, $h = 50$ nm and (a) $a_{\parallel} = 400$ nm, $a_{\perp} = 820$ nm; (b) $a_{\parallel} = 600$ nm, $a_{\perp} = 400$ nm.

of the incident angle causes a blueshift of $\lambda^{\mathrm{sub}}_{(+1,0)}$ and a redshift of $\lambda^{\mathrm{sub}}_{(-1,0)}$, since these diffraction orders are parallel to the in-plane vector of the incident light. According to Eq. (3), $\lambda^{\mathrm{sub}}_{(+1,0)}$ is proportional to $(1 - \sin\theta)$, while $\lambda^{\mathrm{sub}}_{(-1,0)}$ is proportional to $(1 + \sin\theta)$. The dispersion relations of the diffraction orders are calculated and plotted in Fig. 5(b), which matches with the simulation results very well. Specifically, the redshift of $\lambda^{\mathrm{sup}}_{(-1,0)}$ by increasing the incident angle enhances its wavelength sensitivity to the superstrate refractive index for applications of plasmonic sensors. At a large incident angle, two new plasmonic modes at 600 and 670 nm are observed in Fig. 5(b), which correspond to the out-of-plane resonances, i.e., the ridge-to-ridge resonance and ridge-to-face resonance.

In conclusion, we have demonstrated that the Au NBAs support multiple plasmonic-photonic couplings that are robust and highly tunable in an asymmetric environment. The subnanoparticle engineering of the plasmonic "hot spots" through simply controlling the depth-to-diameter aspect ratio of the nanobeakers allows the coupling of LSPRs with different diffraction orders to achieve the multiple LPRs. By confining the "hot spots" within the substrates, a robust coupling is maintained for different sizes of the nanobeaker in an asymmetric environment with the resonance wavelength tunable from visible to near-infrared. The different dispersion relations between the orthogonal and parallel coupling are also discussed. These NBAs can be fabricated by selective chemical deposition of Au thin films onto the side walls and bottoms of the nanoholes. E-beam lithography can be applied to fabricate the nanohole arrays in the substrates followed by the deposition of Au. The e-beam resist will be removed after the deposition of Au to avoid the Au coating on the top surfaces of the substrates surrounding the nanoholes. This study opens up a new opportunity for the optimization of plasmonic-photonic coupling through synergizing the subnanoparticle engineering of "hot spots" with the far-field diffractive coupling. The coupling between the superstrate diffraction orders and the plasmonic "hot spots" provides the opportunity for biosensors that can detect target analytes with a broad range of refractive indices. The coupling-enhanced electrical field will also find applications in plasmonic lasers.

The authors acknowledge the financial support of the startup grant from the Cockrell School of Engineering at the University of Texas at Austin and the Beckman Young Investigator Program. We also acknowledge the Texas Advanced Computing Center (TACC) at The University of Texas at Austin for providing HPC resources (URL: http://www.tacc.utexas.edu). We thank B. Bangalore Rajeeva, X. Peng, M. Wang, and Z. Wu for providing helpful discussions on the simulation results and proofreading the manuscript.

References

1. K. A. Willets and R. P. Van Duyne, Annu. Rev. Phys. Chem. **58**, 267 (2007).
2. N. J. Halas, S. Lal, W. S. Chang, S. Link, and P. Nordlander, Chem. Rev. **111**, 3913 (2011).
3. X. Dang, J. Qi, M. T. Klug, P.-Y. Chen, D. S. Yun, N. X. Fang, P. T. Hammond, and A. M. Belcher, Nano Lett. **13**, 637 (2013).
4. D. Lu, J. J. Kan, E. E. Fullerton, and Z. Liu, Nat. Nanotechnol. **9**, 48 (2014).
5. C. Zhao, J. Zhang, and Y. Liu, EPJ Appl. Metamater. **1**, 6 (2014).
6. S. M. Morton, D. W. Silverstein, and L. Jensen, Chem. Rev. **111**, 3962 (2011).
7. V. A. Markel, J. Mod. Opt. **40**, 2281 (1993).
8. S. L. Zou, N. Janel, and G. C. Schatz, J. Chem. Phys. **120**, 10871 (2004).
9. S. L. Zou and G. C. Schatz, J. Chem. Phys. **121**, 12606 (2004).
10. V. A. Markel, J. Phys. B **38**, L115 (2005).
11. W. Zhou and T. W. Odom, Nat. Nanotechnol. **6**, 423 (2011).
12. A. I. Väkeväinen, R. J. Moerland, H. T. Rekola, A. P. Eskelinen, J. P. Martikainen, D. H. Kim, and P. Törmä, Nano Lett. **14**, 1721 (2014).
13. L. Lin and Y. Yi, Opt. Lett. **39**, 4823 (2014).
14. L. Lin and Y. Yi, Opt. Express **23**, 130 (2015).
15. A. G. Nikitin, Appl. Phys. Lett. **104**, 061107 (2014).
16. A. Vitrey, L. Aigouy, P. Prieto, J. M. García-Martín, and M. U. González, Nano Lett. **14**, 2079 (2014).
17. B. Auguie and W. L. Barnes, Phys. Rev. Lett. **101**, 143902 (2008).
18. Y. Chu, E. Schonbrun, T. Yang, and K. B. Crozier, Appl. Phys. Lett. **93**, 181108 (2008).
19. V. G. Kravets, F. Schedin, and A. N. Grigorenko, Phys. Rev. Lett. **101**, 087403 (2008).
20. A. G. Nikitin, A. V. Kabashin, and H. Dallaporta, Opt. Express **20**, 27941 (2012).
21. F. van Beijnum, P. J. van Veldhoven, E. J. Geluk, M. J. A. de Dood, G. W. 't Hooft, and M. P. van Exter, Phys. Rev. Lett. **110**, 206802 (2013).
22. W. Zhou, M. Dridi, J. Y. Suh, C. H. Kim, D. T. Co, M. R. Wasielewski, G. C. Schatz, and T. W. Odom, Nat. Nanotechnol. **8**, 506 (2013).
23. A. I. Kuznetsov, A. B. Evlyukhin, M. R. Goncalves, C. Reinhardt, A. Koroleva, M. L. Arnedillo, R. Kiyan, O. Marti, and B. N. Chichkov, ACS Nano **5**, 4843 (2011).
24. P. Offermans, M. C. Schaafsma, S. R. K. Rodriguez, Y. Zhang, M. Crego-Calama, S. H. Brongersma, and J. G. Rivas, ACS Nano **5**, 5151 (2011).
25. Y. Shen, J. Zhou, T. Liu, Y. Tao, R. Jiang, M. Liu, G. Xiao, J. Zhu, Z.-K. Zhou, X. Wang, C. Jin, and J. Wang, Nat. Commun. **4**, 2381 (2013).
26. B. Auguie, X. M. Bendana, W. L. Barnes, and F. J. Garcia de Abajo, Phys. Rev. B **82**, 155447 (2010).
27. A. G. Nikitin, T. Nguyen, and H. Dallaporta, Appl. Phys. Lett. **102**, 221116 (2013).
28. W. L. Barnes, W. A. Murray, J. Dintinger, E. Devaux, and T. W. Ebbesen, Phys. Rev. Lett. **92**, 107401 (2004).
29. J. Henzie, M. H. Lee, and T. W. Odom, Nat. Nanotechnol. **2**, 549 (2007).
30. P. Johnson and R. Christy, Phys. Rev. B **6**, 4370 (1972).
31. M. Meier, A. Wokaun, and P. F. Liao, J. Opt. Soc. Am. B **2**, 931 (1985).